

Supporting Information

Optical and electrochemical effects of H₂ and O₂ bubbles at upward-facing Si photoelectrodes

Paul A. Kempler¹, Zachary P. Ifkovits¹, Weilai Yu,¹ Azhar I. Carim,¹ Nathan S. Lewis^{1,2*}

¹Division of Chemistry and Chemical Engineering, 127-72, 210 Noyes Laboratory, California Institute of Technology, Pasadena, CA 91125

²Beckman Institute, California Institute of Technology, Pasadena, CA 91125

*Corresponding Author: nslewis@caltech.edu

Materials: All chemicals were commercially available and used as received. Potassium ferrocyanide(II) trihydrate ($K_4Fe(CN)_6$, ACS Reagent 99%), was obtained from Aldrich, gallium-indium eutectic (GaIn, 99.99%, metals basis) was obtained from Alfa Aesar, and concentrated ammonium hydroxide (NH_4OH , 28%-30%) was obtained from JT Baker. Hydrochloric acid (HCl, ACS grade 36.5-38%), acetone, and isopropyl alcohol were obtained from Millipore. Buffered oxide etchant (6:1 (v/v) 40% NH_4F to 49% HF) was obtained from Transene Inc and hydrogen peroxide (H_2O_2 , ACS grade 30%) was obtained from Macron Chemicals. Sulfuric acid (H_2SO_4 , TraceMetal grade) was obtained from Fisher Scientific and potassium hydroxide (KOH, 99.98% metals basis) was obtained from ACROS Organics. Solutions were diluted to the specified concentration with water having a resistivity of 18.2 $M\Omega\cdot cm$, obtained from a Millipore deionized (DI) water system. N-type Si wafers with a resistivity of 0.4 $\Omega\cdot cm$ and p-type Si wafers with a resistivity of 10–20 $\Omega\cdot cm$, having diameters of 100 mm, thicknesses of 525 μm , and $\langle 100 \rangle$ orientation, were obtained from Addison Engineering. Fumasep FAAM-15 and NafionTM 117 were obtained from Fuel Cell Store and nickel wire (Ni, 99.5%) with a diameter of 0.5 mm, was obtained from BeanTown Chemical. Calomel (CHI150) and mercurous oxide (CHI152) reference electrodes were obtained from CH Instruments.

Preparation of μW substrates: Silicon wafers were cleaned with acetone and isopropyl alcohol, exposed to a hexamethyldisilazane primer, and spin-coated with S1813 photoresist (Shipley) at 4000 rpm. The resist layer was photolithographically patterned via UV-exposure through a chrome mask which had a square grid of circular holes 6 μm in diameter and 14 or 28 μm in spacing. Al_2O_3 etch masks, 125 nm in thickness, were evaporated into the exposed hole array via electron beam evaporation at 1 $\text{\AA} s^{-1}$. Substrates were cleaved, mounted onto a 6 in diameter Si

carrier wafer with thermally conductive oil, and loaded into an Oxford Instruments Dielectric System 100 ICP-RIE. Microwires were formed via deep reactive-ion etching, DRIE, of Si at -120-130°C in a SF₆/O₂ plasma at a capacitively coupled power of 3 W and an inductively coupled power of 900 W. Silicon was cleaned prior to metallization via a modified Radio Corporation of America (RCA) standard clean 1 (5:1:1 (vol) H₂O:NH₄OH:H₂O₂ at 70-75 °C) for at least 10 min followed by an RCA standard clean 2 (6:1:1 (vol) H₂O:HCl:H₂O₂ at 65-70 °C) for at least 10 min. The samples were dipped in HF between the cleaning steps, which also resulted in the removal of the Al₂O₃ etch mask.

Fabrication of electrodes: Metallization was performed in an Orion Series Sputtering system (AJA) at a base pressure of 10⁻⁷ torr. Ni was sputtered in a 5 mtorr Ar plasma at a deposition rate of ~1.5 nm min⁻¹. An ohmic back contact was made to the rear side of the Si with an In-Ga eutectic (Alfa Aesar), and the electrode was affixed to a Cu-Sn wire via conductive Ni or Ag epoxy (Ted Pella). The electrode was sealed into a piece of 6 mm diameter borosilicate glass tubing using a chemically resistant epoxy (Hysol 9460) that was cured for >12 h at room temperature. The electrode areas were measured in ImageJ with a ruler serving as a scale bar.

Scanning-electron microscopy: Scanning-electron micrographs (SEMs) were obtained with a FEI Nova NanoSEM 450 at an accelerating voltage of 10.00 kV with a working distance of 5 mm and an in-lens secondary electron detector. Plan-view SEMs were acquired with a resolution of 14 pixels μm⁻¹. Cross-sectional SEMs were acquired from perspective 85° away from the substrate normal with a resolution of 21 pixels μm⁻¹.

Mass-transport velocity measurements: The current derived from oxidation of Fe(CN)₆⁴⁻ was calculated based on the change in absorptivity of the electrolyte in the cell before vs after a bulk electrolysis. The electrolyte was not stirred during testing but was vigorously stirred by a

magnetically-powered Teflon stir bar prior to sampling the electrolyte. A calibration was performed at a large area Ni coil held potentiostatically at 1.3 V vs RHE. At this potential, the current associated with oxygen evolution was negligible and the current derived from $\text{Fe}(\text{CN})_6^{4-}$ oxidation was limited by mass transport. **Figure S7** presents the change in absorptivity at 420 nm as a function of charge passed for a series of such experiments. The concentration of $\text{Fe}(\text{CN})_6^{3-}$ in the cell was calculated as Q / nFV where Q is the total charge passed at 1.3 V vs. RHE, n is the number of electrons required for the oxidation (1), F is Faraday's constant (96485 C mol^{-1}) and V is the volume of electrolyte in the cell during oxidation (0.097 L or 0.047 L for cells incorporating the upward-facing and downward-facing electrodes, respectively). The extinction coefficient of $1059 \text{ M}^{-1} \text{ cm}^{-1}$ was calculated from a linear regression of the measured absorbances and calculated concentrations.

Sample characterization: Absorbance spectra were collected on a Agilent 8453 UV-vis Spectrometer using polystyrene cuvettes with a path length of 1 cm. Optical constants were measured by use of a variable-angle spectroscopic ellipsometer with a rotating analyzer (J.A. Woolam Co., Inc.). Measurements were recorded at angles of incidence of 60° , 65° , and 70° in 5 nm increments in wavelength over a range from 300 to 1000 nm. Reflectance coefficients were calculated from the best-fit optical constants and thicknesses for the films.

Image processing: Images of downward-facing photoelectrodes were processed in MATLAB. The manually defined electrode area restricted the pixel area for data collection and was used to calibrate the pixels per mm^2 scale at the electrode surface. The location and diameter of bubbles were recorded for each image, and the fractional coverage was calculated relative to the geometric electrode area. Manual quantification of bubbles was supplemented by automatic detection of similarly sized bubbles using a Hough transform.

Convection due to thermal gradients: A solar fuels devices exhibiting absorbing 90% of the solar spectrum and converting solar energy to fuel at an efficiency of 10% will require an outgoing flux of $8.1 \times 10^2 \text{ W m}^{-2}$ of radiation and heat at steady state. In the absence of bubble-driven convection, this heat will be removed by conduction across temperature gradients and convection due to resulting density gradients. The maximum temperature gradient expected to occur for a large area, planar absorber, can be found using Fourier's Law, assuming temperature drops uniformly across the 0.01 m thick electrolyte layer (Equation S1)

$$q = -k \frac{dT}{dz} \quad (\text{S1})$$

Where q is the heat flux in W m^{-2} , T is the temperature in the electrolyte in K, k is the thermal conductivity of water, $0.60 \text{ W m}^{-1} \text{ K}^{-1}$, and z is the thickness coordinate extending positively from zero at the surface of the top-facing light absorber. A temperature gradient of 14 K across a 0.01 m electrolyte layer will sustain the removal of $8.1 \times 10^2 \text{ W m}^{-2}$ of heat via conduction alone. The relative contribution of thermal convection to conduction across a layer of thickness L with temperature difference ΔT is given by the Rayleigh number, Ra (Equation S2),

$$Ra = \frac{gL^3\beta\Delta T}{\alpha\nu} \quad (\text{S2})$$

where g is the acceleration due to gravity (9.81 m s^{-2}), β is the thermal expansion coefficient ($210 \times 10^{-6} \text{ K}^{-1}$), α is the thermal diffusivity ($0.14 \times 10^{-6} \text{ m}^2 \text{ s}^{-1}$), and ν is the kinematic viscosity ($1.00 \times 10^{-3} \text{ Pa} \cdot \text{s}$). A fluid layer between a solid surface and a free surface is predicted to be stable for $Ra < 1101$.¹ Ra is 200 for a 0.01 m liquid layer above an absorber surface that is 14 K greater than the ambient temperature, indicating that the fluid layer will likely be stable. Increased thicknesses of the liquid layer or increased irradiance could lead to $Ra > 1101$ such that thermal convection cannot be ignored.

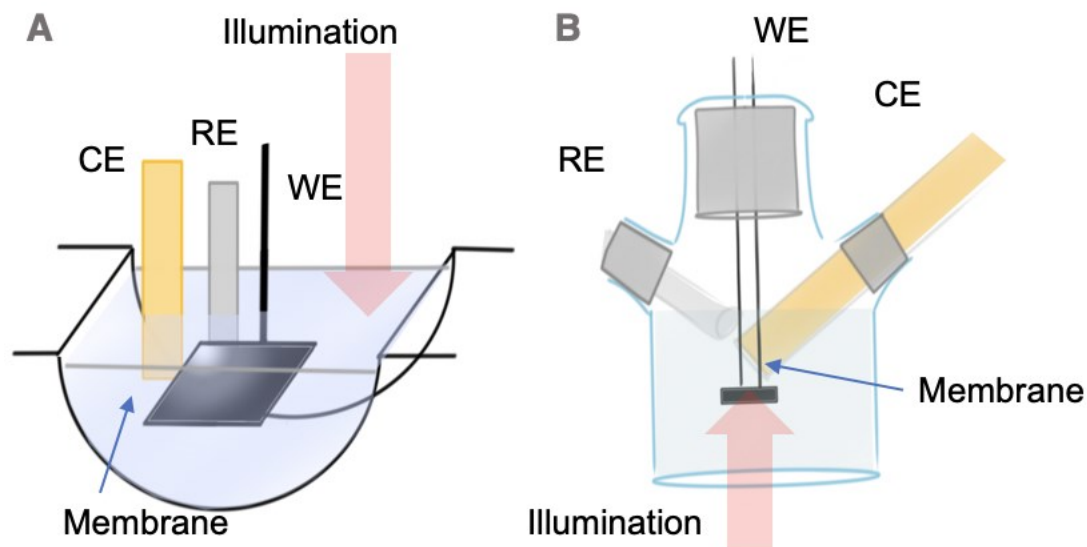


Figure S1: Schemes of cells used for (A) upward-facing and (B) downward-facing photoelectrochemical experiments in 0.50 M $\text{H}_2\text{SO}_4(\text{aq})$ and 1.0 M $\text{KOH}(\text{aq})$.

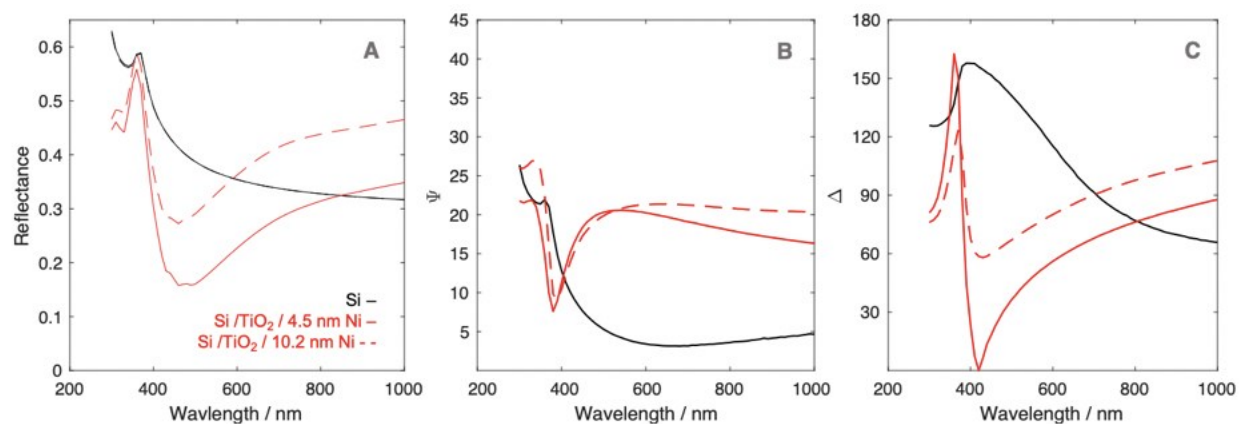


Figure S2: (A) Calculated spectral reflectance of Si, black line, Si/TiO₂(46 nm)/Ni(4.5 nm), red line, and Si/TiO₂(46 nm)/Ni(10.2 nm), red dashed-line, surfaces in air. Film thickness and spectral reflectance was calculated from measured (B) ψ (B) and (C) Δ .

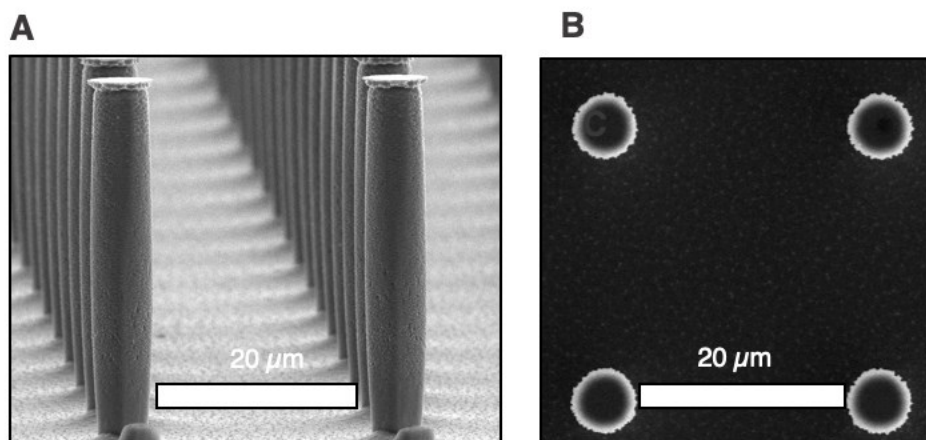


Figure S3: (A) Cross-sectional scanning-electron micrograph of a μW n-Si/TiO₂/Ni sample. (B) Plan-view scanning-electron micrograph of a μW n-Si/TiO₂/Ni sample.

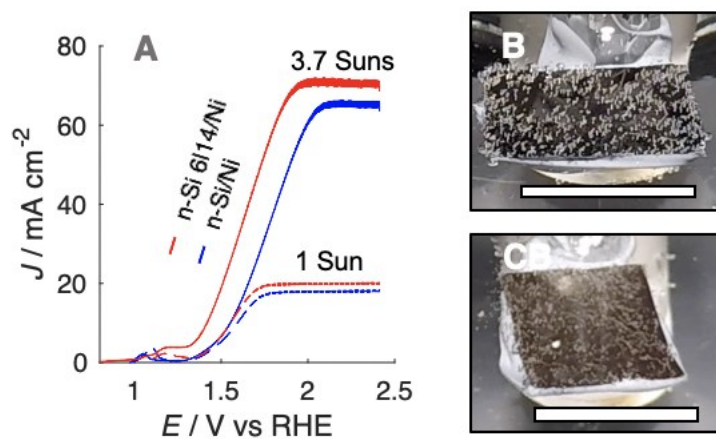


Figure S4: (A) J - E behavior for upward-facing n-Si/TiO₂/Ni photoanodes in stagnant 1.0 M KOH(aq) recorded at 200 mV s⁻¹ under illumination from an ELH lamp. (B) Photographs of a planar n-Si/TiO₂/Ni electrode at 60 mA cm⁻² (C) μW 6|14 n-Si/TiO₂/Ni electrode at 65 mA cm⁻² Scale bars represent 1 cm.

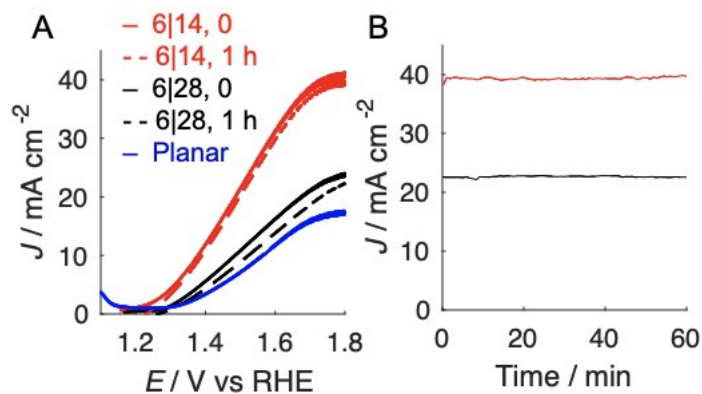


Figure S5: (A) J - E behavior for μ W 6|14 (red) and μ W 6|28 (black) upward-facing n-Si/TiO₂/Ni photoanodes in stagnant 1.0 M KOH(aq) recorded at 200 mV s⁻¹ under illumination from an ELH lamp. Forward scans were recorded before (continuous) and reverse scans were recorded after (dashed) 1 hour of continuous O₂ evolution at 1.8 V vs RHE. A planar n-Si/TiO₂/Ni photoanode with 10 nm of Ni is shown in blue for comparison of the optical properties of the thicker Ni films (B) J - t behavior for μ W 6|14 and μ W 6|28 photoanodes in (A) held at 1.6 V vs RHE.

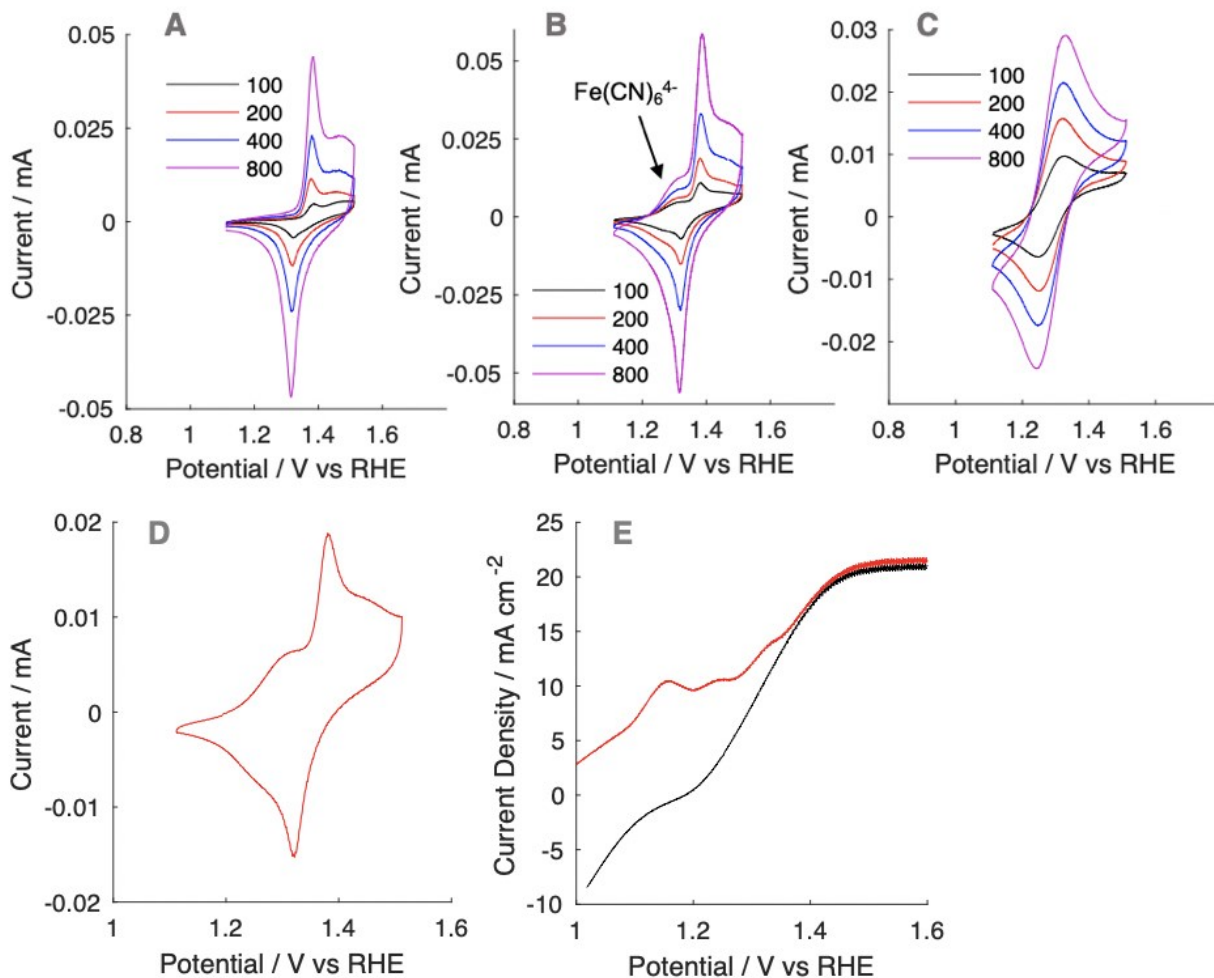


Figure S6: (A) Cyclic voltammogram of a polished, 0.5 mm diameter Ni wire embedded in epoxy in 1.0 M KOH(aq). The scan rate is specified in mV s^{-1} . (B) Cyclic voltammogram of 10 mM $\text{Fe}(\text{CN})_6^{4-}$ in 1.0 M KOH(aq) at a polished, 0.5 mm diameter Ni wire embedded in epoxy. (C) Cyclic voltammogram of 10 mM $\text{Fe}(\text{CN})_6^{4-}$ in 1.0 M KOH(aq) at a Au wire embedded in borosilicate glass tubing. (D) Expanded view of voltammetry of 10 mM $\text{Fe}(\text{CN})_6^{4-}$ in 1.0 M KOH(aq) at a polished, 0.5 mm diameter Ni wire embedded in epoxy at a scan rate of 200 mV s^{-1} . (E) Linear sweep voltammograms recorded at an upward-facing μW 6|28 n-Si/TiO₂/Ni photoanode under illumination from a 630 nm light-emitting diode before (red) and after (black) a constant potential hold at 1.5 V vs RHE for 5 min.

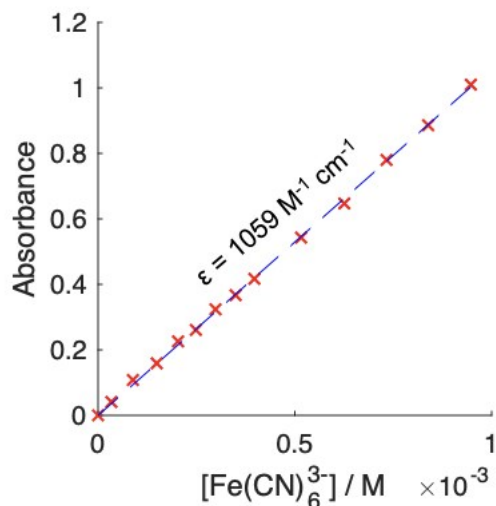


Figure S7: Electrolyte absorbance at 420 nm versus $[\text{Fe}(\text{CN})_6^{3-}]$ as measured via the anodic charge passed at a Ni wire in a solution of 10 mM $\text{Fe}(\text{CN})_6^{4-}$ in 1.0 M $\text{KOH}(\text{aq})$.

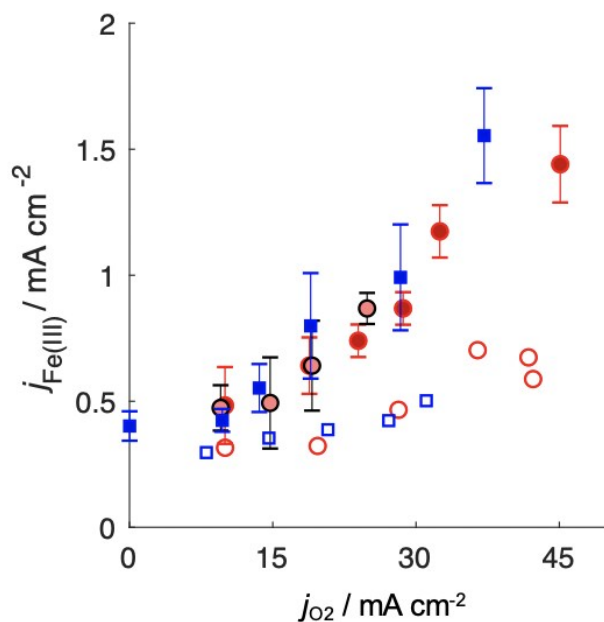


Figure S8: Calculated $j_{\text{Fe(III)}}$ as a function of j_{O_2} as measured via quantification of $\text{Fe}(\text{CN})_6^{3-}$ before and after bulk electrolysis in 10 mM $\text{Fe}(\text{CN})_6^{4-}$, 1.0 M $\text{KOH}(\text{aq})$. Measurements at planar, blue squares, $\mu\text{W } 6|14$, dark-red circles, and $\mu\text{W } 6|28$ light-red circles, n-Si/ TiO_2/Ni . Upward-facing measurements are represented as filled markers, downward-facing measurements as open markers. Error bars represent one standard deviation from three independent experiments.



Figure S9: Unaltered side-view photographs of illuminated gas streams emanating from upward-facing photoanodes at $J_{\text{ph}} = 20 \text{ mA cm}^{-2}$.

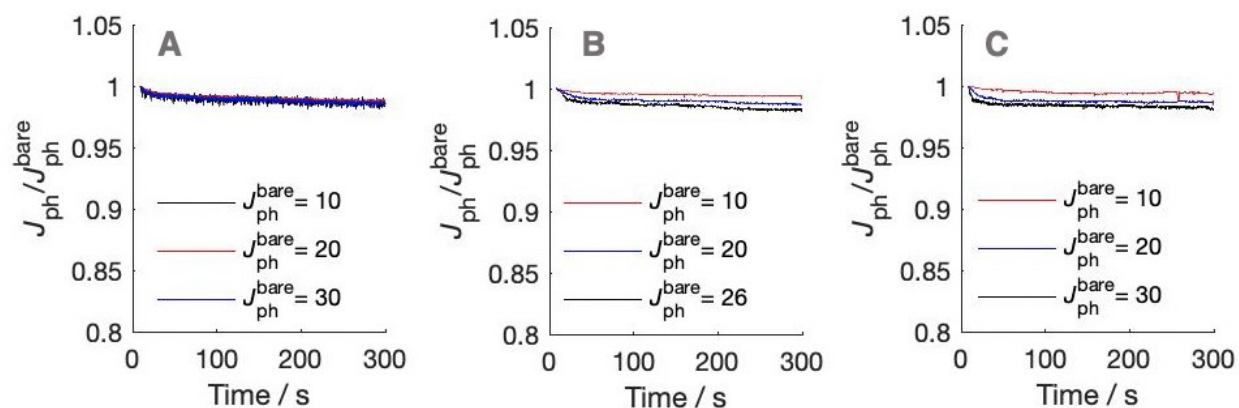


Figure S10: Time-dependent $J_{\text{ph}}/J_{\text{ph}}^{\text{bare}}$ behavior for planar (A), $\mu\text{W } 6|28$ (B), and $\mu\text{W } 6|14$ (C) n-Si/TiO₂/Ni electrodes in 10 mM Fe(CN)₆⁴⁻(aq), 1.0 M KOH(aq) as a function of illumination intensity. Optical losses did not exceed 2% of the maximum photocurrent.

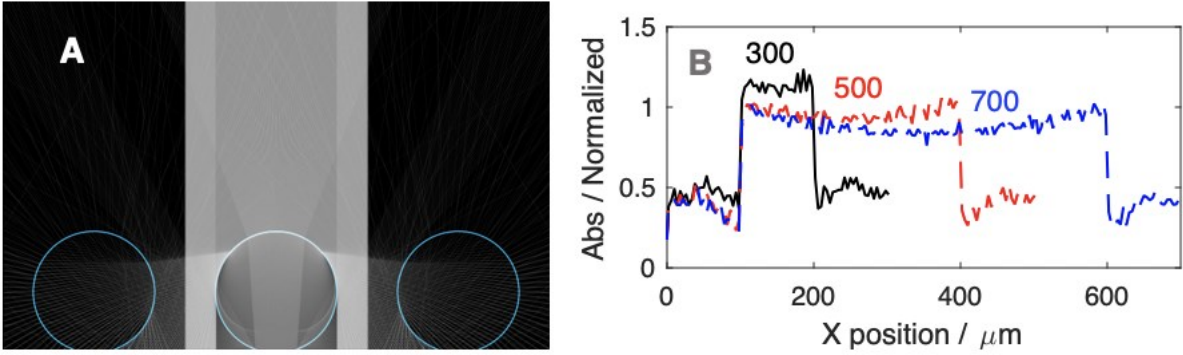


Figure S11: (A) Ray-tracing simulation for multiple surface-attached gas bubbles with $\theta_b = 160^\circ$. (B) Optical absorption distribution at a surface containing bubbles with $R_b = 100 \mu\text{m}$ and $\theta_b = 160^\circ$ for varied center to center distances, recorded as a function of position. The absorption at individual positions, as bins, was normalized to the total power incident on each bin in the absence of reflections or refractions.

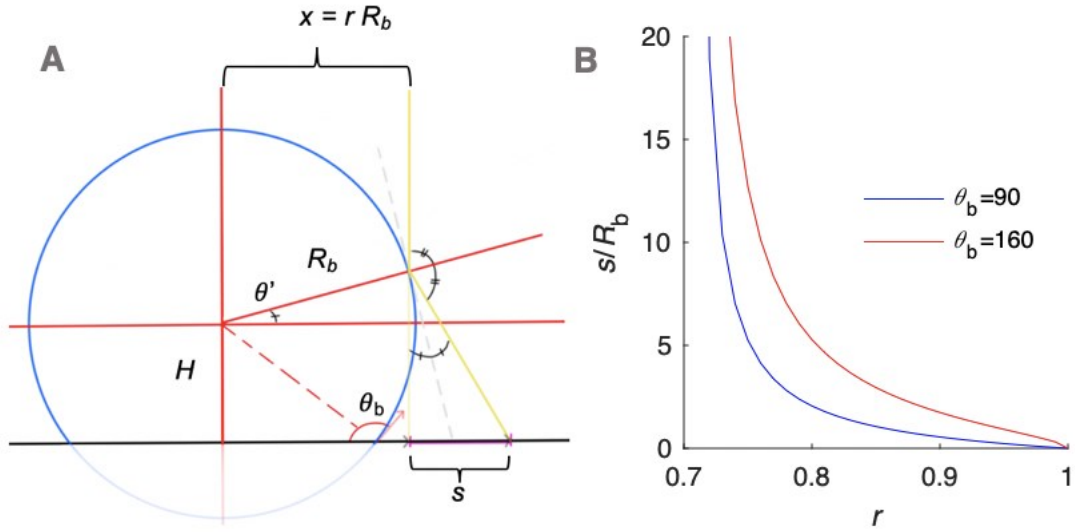


Figure S12: (A) Graphical representation of Equation 2. (B) Plot of the dimensionless scattering distance (s/R) versus the ray position ($r = x/R$) for bubbles with $\theta_b = 90^\circ$ and 160° .

The scattered distance, $s(r)$, can be determined from the scattered angle off normal incidence and height of the ray intersection off the absorber surface. This height can be calculated as the sum of H and $R_b \sin(\theta')$, where

$$H = R_b \sin\left(\theta_b - \frac{\pi}{2}\right)$$

such that

$$s = R_b (\sin \theta' - \cos \theta_b) \tan 2\theta'$$

To allow easier integration on the projected plane of incident the equation can be expressed in terms of r , using the fact that $r = R_b \cos(\theta_b)$ and $\sin(\theta_b) = (1 - r^2)$.

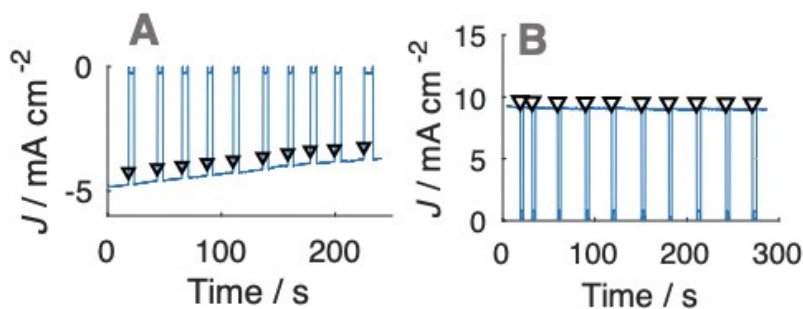


Figure S13: (A) J - t behavior of an inverted p-Si/H electrode under chopped illumination. The light source was turned off and an image was recorded under diffuse light at times marked with arrows. (B) J - t behavior of an inverted n-Si 6|14 electrode under chopped illumination.

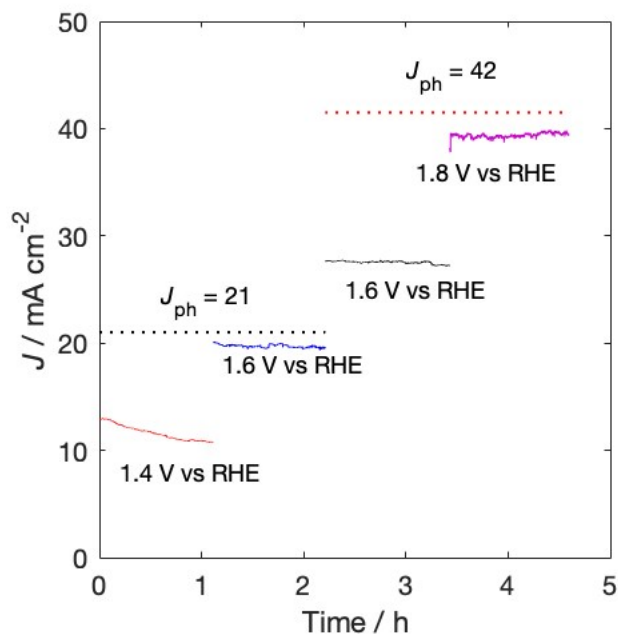


Figure S14: Extended J vs t data for a n-Si 6|14/TiO₂/Ni photoanode under 1-Sun (dotted black) and 2-Suns (dotted red) illumination in 1.0 M KOH(aq). The potential was stepped from 1.4 V (solid red), to 1.6 (solid blue, black), to 1.8 V vs RHE (solid purple). Sweeps to measure J_{ph} were recorded before and after individual constant potential holds.

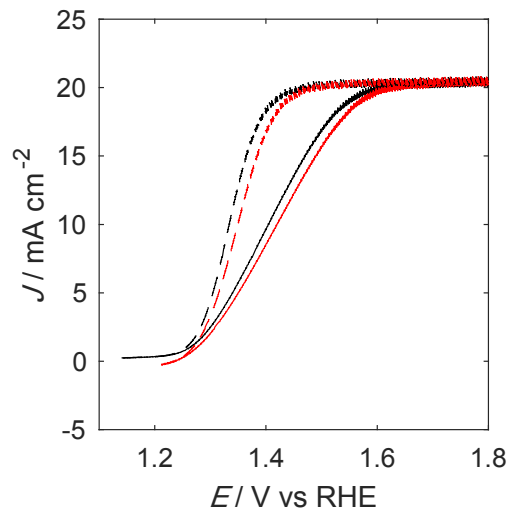


Figure S15: iR -corrected J vs E behavior of an n-Si/TiO₂/Ni photoanode in 1.0 M KOH(aq) under illumination from an ELH lamp. The forward and reverse sweeps were recorded before (black) and after (red) a 1 hr constant potential hold at 1.6 V vs. RHE. Original data and data corrected for the iR potential are shown as continuous and dashed lines, respectively.

References

1. W. M. Deen, *Analysis of Transport Phenomena*, Oxford University Press, Oxford, 1998